Available online at www.sciencedirect.com
SCIENCE DIRECT®
Journal of Colloid and Interface Science 297 (2006) 665–671
JOURNAL OF Colloid and Interface Science
www.elsevier.com/locate/jcis

Inner-sphere adsorption geometry of Se(IV) at the hematite (100)–water interface

Jeffrey G. Catalano [a,*], Zhan Zhang [a], Paul Fenter [a], Michael J. Bedzyk [a,b]

[a] *Argonne National Laboratory, 9700 South Cass Avenue, Argonne, IL 60439, USA*
[b] *Northwestern University, Evanston, IL 60208, USA*

Received 11 October 2005; accepted 9 November 2005

Available online 28 December 2005

Abstract

The 3-dimensional structure of adsorption complexes on mineral surfaces provides insight into the fundamental mechanisms controlling sorption processes. This is important to the development of a general understanding of the behavior of contaminants such as selenite in the environment. The adsorption of selenite (SeO_3^{2-}) on the hematite (100) surface was studied using X-ray standing wave (XSW) measurements. Inner-sphere bidentate surface complexes bridging between adjacent singly-coordinated oxygen sites were identified as the primary adsorption site. The lack of binding to doubly-coordinated oxygen sites that were also exposed on the surface was likely due to differences in the reactivity or exchange kinetics of these sites or cation–cation repulsion, although the latter appears to be a secondary effect based on past observations. While these bridging bidentate geometries are similar to those inferred in past spectroscopic studies, the Se–Fe distances are such that these species might be misidentified as edge-sharing complexes if studied by EXAFS spectroscopy, highlighting the need for a fundamental understanding of mineral surface structure.

Keywords: Selenite; Hematite; Inner-sphere adsorption; XSW

1. Introduction

Adsorption of contaminants and trace element ions onto mineral surfaces often controls the transport and cycling of these elements in the environment [1]. Surface complexation models are often used to describe the macroscopic adsorption behavior of elements as a function of solution parameters such as element concentration, pH, ionic strength, etc. The chemical reactions used in surface complexation models can be evaluated by investigating the structure and composition of the proposed surface complexes spectroscopically. However, many commonly used spectroscopic methods provide indirect (e.g., vibrational spectroscopy) or 1-dimensional (e.g., X-ray absorption spectroscopy) information on the registry of adsorbed ions with respect to the structure of the adsorbent. Unambiguous determination of surface complex structure using such methods is often not possible as assumptions must be made regarding the available binding sites and possible adsorption geometries.

A more fundamental picture of surface complexes may be obtained by studying the adsorption of ions onto single crystal surfaces, as these phases are amenable to surface-specific probes that are capable of determining the 3-dimensional relationship of adsorption complexes to mineral surface structures. The type and distribution of potential sites of adsorption on single crystal surfaces can be measured experimentally using surface X-ray scattering. Surface X-ray scattering or Bragg-reflection X-ray standing wave (XSW) measurements can then be used to determine the site(s) of adsorption with respect to the crystal lattice of the adsorbent mineral. Such methods have been used to study ion adsorption onto calcite [2–8], corundum [9], hematite [9,10], and rutile [11–13].

In this study we investigated the (inner-sphere) adsorption of selenite (SeO_3^{2-}) on the (100) surface of hematite (α-Fe_2O_3) using XSW measurements. Selenium is toxic at high concentrations and has been implicated in teratogenic effects observed in wildlife at the Kesterson National Wildlife Refuge in Califor-

* Corresponding author. Fax: +1 630 252 7415.
E-mail address: catalano@anl.gov (J.G. Catalano).

0021-9797/$ – see front matter
doi:10.1016/j.jcis.2005.11.026

nia [14]. In oxidizing environments selenium occurs primarily as the selenite (SeO_3^{2-}) and selenate (SeO_4^{2-}) oxoanions. Selenite adsorbs strongly to mineral surfaces [15–30], typically forming inner-sphere bidentate adsorption complexes on metal oxide surfaces [31–34].

2. Materials and methods

2.1. Sample preparation

Hematite single crystals oriented, cut, and polished parallel to (100) were obtained from Commercial Crystal Laboratories (Naples, FL). Prior to use, the crystals were cleaned by repeated rinsing with HPLC-grade acetone and methanol, rinsing with deionized water (>18 MΩ cm), soaking for 5 min each in 10^{-3} M NaOH and 10^{-3} M HCl with deionized water rinses in between, and finally soaking in deionized water. To reduce the adventitious carbon on the surface, the crystals were blown dry in a stream of Ar gas, and then heated in an oven at 275 °C for 3 h. After cooling, the crystals were stored in deionized water until use. Preliminary X-ray reflectivity measurements (not shown) provide an estimated surface roughness of ∼30 Å, comparable to the 25 Å roughness seen for the (001) surface of hematite [35].

Solutions of 10 and 100 μM $Na_2SeO_3{\cdot}5H_2O$ in 10 mM NaCl were prepared from reagent grade chemicals and deionized water; the pH was adjusted to 4 with HCl. A hematite (100) single crystal was loaded in deionized water into a sample cell and sealed with 8 μm-thick Kapton film. After mounting the sample on a four-circle spectrometer (details below), the reaction solution was exchanged into the cell and allowed to react for 10 min, after which it was drained from the cell, leaving a thin solution film on the crystal surface (estimated to be ∼2 μm thick based on past studies [36]). This cycle was repeated for approximately one hour, after which the cell was sealed. XSW measurements were made for hematite (100) reacted with the 10 and 100 μM Se(IV) solutions. All measurements were made in situ in approximately 30 h.

2.2. X-ray standing wave measurements and analysis

XSW measurements were performed in a vertical scattering geometry on a four-circle spectrometer at beamline 12-ID-D (BESSRC) of the Advanced Photon Source, Argonne National Laboratory. The incident X-ray energy (15.048 keV) was selected using a liquid N_2-cooled, symmetrical Si (111) monochromator. The incident beam dispersion was controlled using two sets of Si (111) or (220) double-bounce, channel cut post-monochromators. The beam size was typically 0.01 mm^2. Fe and Se$K\alpha$ X-ray fluorescence was measured using a single-element energy dispersive Ge detector mounted horizontally facing the polarization direction of the incident X-ray beam. Se surface coverage was measured by comparison of the Se$K\alpha$ X-ray fluorescence from the sample with the Zn$K\alpha$ X-ray fluorescence from a standard of known Zn concentration; corrections were made for differences in X-ray absorption cross section, fluorescence yield, and linear attenuation.

Details of XSW measurements and the determination of adsorbate positions on mineral surfaces can be found in Bedzyk and Cheng [37]. Briefly, the reflectivity, $R(\theta)$, and the X-ray fluorescence yields, $Y(\theta)$, were measured simultaneously by rocking the hematite crystal through the specified Bragg reflection from the low-angle to the high-angle side. The resulting modulation of $Y(\theta)$ for the element of interest provides information on the location of the atom with respect to the diffracting plane. For an adsorbate, this modulation takes the form:

$$Y(\theta) = Y_{\mathrm{OB}}\Big[1 + R(\theta) + 2\sqrt{R(\theta)}\, f_H \cos\big(\nu(\theta) - 2\pi P_H\big)\Big], \quad (1)$$

where Y_{OB} is the fluorescence yield at an off-Bragg angle, $\nu(\theta)$ is the relative phase of the standing wave field, and H is the diffraction vector. The coherent position, P_H, is the average fractional position, $\Delta\mathrm{d}/\mathrm{d}_H$, of the adsorbate ion with respect to the diffracting plane (e.g., an adsorbate ion at a distance above the diffracting plane equaling half the d-spacing, or $\Delta\mathrm{d}/\mathrm{d}_H = 0.5$, has a $P_H = 0.5$). The coherent fraction, f_H, is a measure of the spatial distribution of the fluorescing ion, and is comprised of three terms:

$$f_H = CaD, \quad (2)$$

where C is the ordered fraction of the fluorescing element, a is a geometrical factor taking into account the effects of multiple ion positions, and D is the Debye–Waller factor. In practice, P_H and f_H are obtained through fitting Eq. (1) to the experimental $Y(\theta)$.

The Fe fluorescent modulations were dominated by strong extinction effects (observed as an overall reduction in fluorescent intensity near the Bragg condition) that resulted from using a large take-off angle between the detector and the crystal surface. As a result, the measurements were not sensitive to P_H since the Fe$K\alpha$ escape depth was much larger than the extinction depth. Instead, the Fe coherent positions were fixed to their crystallographic values in the analysis, which included the effect of extinction. This will be remedied in the future by using a small (<3°) take-off angle for detecting fluorescent X-rays.

P_H and f_H are also the phase and amplitude, respectively, of the Hth Fourier coefficient, $\mathscr{F}_H$, of the element-specific normalized density profile, $\rho(\mathbf{r})$:

$$\mathscr{F}_H = \int \rho(\mathbf{r}) \exp(i2\pi \boldsymbol{H}\cdot\mathbf{r})\,\mathrm{d}\mathbf{r} = f_H \exp(i2\pi P_H). \quad (3)$$

As recently demonstrated [38], the full elemental distribution, $\rho(\mathbf{r})$, may be obtained directly by Fourier inversion of the XSW-measured Fourier coefficients in a process called XSW imaging:

$$\begin{aligned}\rho(\mathbf{r}) &= \mathrm{Re}\big[\Sigma_H \mathscr{F}_H \exp(-i2\pi \boldsymbol{H}\cdot\mathbf{r})\big] \\ &= \mathrm{Re}\big[\Sigma_H f_H \exp\big(i2\pi(P_H - \boldsymbol{H}\cdot\mathbf{r})\big)\big]. \quad (4)\end{aligned}$$

The site of Se(IV) adsorption was determined by comparison of the 3-dimensional density profile obtained through Fourier inversion to the structure of the surface unit cell [13].

The Se position with respect to the hematite lattice was further refined using triangulation by least-squares fitting of

the atomic coordinates and ordered fraction, C, of Se as described previously [2–6,12,37]. Differences between the model-optimized f_{opt} and P_{opt} and the experimental f_H and P_H values were minimized using least-squares fitting techniques. A fixed vibrational amplitude of 0.2 Å was used to estimate the Debye–Waller factor, D, of Se.

3. Results and discussion

3.1. Hematite (100) surface structure

The structure of hematite (α-Fe_2O_3) consists of a distorted hexagonal closest packed oxygen layers with Fe^{3+} occupying two thirds of the octahedral holes, trigonal space group $R\bar{3}C$ with lattice parameters $\mathbf{a} = 5.035$ Å, $\mathbf{c} = 13.747$ Å, and $\gamma = 120°$ [39]. For simplicity, *hkl* notation will be used for bulk indices instead of the full *hkil* notation, which is unnecessary as $h + k + i = 0$ for hexagonal systems. The crystal structure of hematite was re-indexed with a rectangular surface unit cell having the c-axis normal to the (100) surface. This allows for easier visualization of surface structure and determination of the reflections that are symmetry equivalent with respect to the bulk but nonequivalent with respect to the (100) surface. For this surface, the rectangular surface unit cell is bound by the bulk crystallographic vectors parallel to [010], [001], and [210] and can be defined with surface lattice parameters $\mathbf{a}_s = 5.035$ Å, $\mathbf{b}_s = 13.747$ Å, $\mathbf{c}_s = 8.721$ Å.

The hematite (100) surface is expected to consist of rows of dimers of iron octahedra along $\mathbf{a}_s$ (Fig. 1). The crystal structure of hematite is such that there is only one chemically-feasible (100) termination. Our choice of indexing produces six chemically-identical, crystallographically-related (100) planes in each surface unit cell. The XSW analyses are independent of which of these six planes are chosen as the surface; an adsorbate (e.g., selenite) bound to any of these planes produces the same coherent positions and fractions if sorbed in the same local adsorption geometry. While there is nothing structural or chemical that requires the dimers of iron octahedra to remain intact (e.g., one of the two iron octahedra could desorb from the surface to reduce Fe–Fe repulsion), the adsorption geometry of selenite observed by XSW imaging (discussed below) is

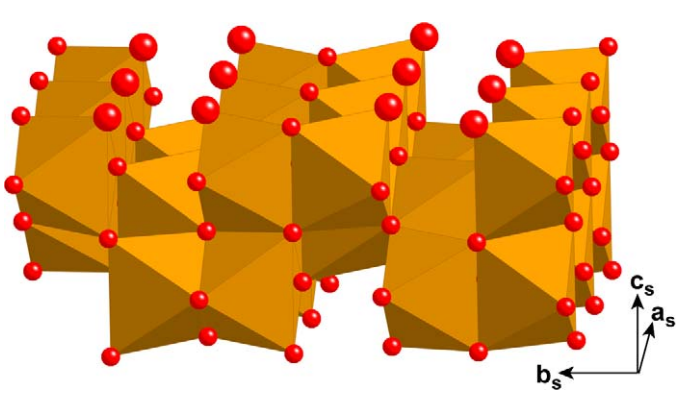

Fig. 1. Polyhedral view of the bulk-terminated hematite (100) surface. The larger spheres are singly-coordinated oxygen sites, which are potential sites of adsorbate binding.

Table 1
XSW measurements of SeO_3^{2-} adsorbed on the hematite (100) surface

Reflection, H (*hkl*)		d_H	q_H	Se		Fe		
Bulk[a]	Surface[b]	(Å)	(Å^{-1})	f_H[c]	P_H[c]	f_H[c]	f_{cal}[d]	P_H[e]
			10 μM Se(IV)					
(1 0 $\bar{2}$)	(0 $\bar{2}$ 2)	3.69	1.71	0.18(2)	0.47(2)	0.19(1)	0.245	0.5
(1 0 4)	(0 4 2)	2.70	2.33	0.27(2)	0.45(1)	0.68(1)	0.88	0.5
(2 $\bar{1}$ 0)	($\bar{1}$ 0 3)	2.52	2.49	0.32(2)	0.81(1)	0.72(2)	1	1
(0 1 2)	(1 2 1)	3.69	1.71	0.24(2)	0.28(1)	0.12(1)	0.245	0.5
(1 $\bar{4}$ $\bar{1}$)	($\bar{1}$ $\bar{4}$ 1)	2.70	2.33	0.14(2)	0.30(1)	0.83(1)	0.88	0.5
			100 μM Se(IV)					
(1 0 $\bar{2}$)	(0 $\bar{2}$ 2)	3.69	1.71	0.09(1)	0.50(3)	0.18(1)	0.245	0.5
(1 0 4)	(0 4 2)	2.70	2.33	0.14(1)	0.48(1)	0.56(1)	0.88	0.5
(2 $\bar{1}$ 0)	($\bar{1}$ 0 3)	2.52	2.49	0.30(1)	0.83(1)	0.81(1)	1	1

[a] Indexing of the bulk structure from Finger and Hazen [37].
[b] Re-indexed with the surface c-axis ($\mathbf{c}_s$) normal to the surface.
[c] The measured coherent fractions and positions with the uncertainties in the last digit in parentheses.
[d] The calculated coherent fractions for Fe atoms based on the bulk hematite single crystal structure assuming $C = 1$ and $D = 1$ (see Eq. (2)).
[e] The Fe coherent positions were fixed to their crystallographic values.

only feasible if these dimers are present. The potentially reactive surface functional groups on this surface are singly- and doubly-coordinated oxygen atoms exposed on the top of the dimers of iron octahedra. The bond valence of these surface oxygen atoms is likely satisfied through hydroxylation and hydrogen bonding when the surface is in contact with aqueous solution.

3.2. Inner-sphere selenite adsorption geometry

The f_H and P_H values derived from the five measured $Y(\theta)_{Se}$ and $Y(\theta)_{Fe}$ (Fig. 2) were used as input to Eq. (4) to determine the position of adsorbed Se with respect to the Fe atom positions in the hematite (100) surface unit cell using the XSW imaging approach (Fig. 3). Surface symmetry equivalents of the measured reflections were included in the inversion by assuming the same f_H and P_H values (no symmetry equivalents were measured). The maximum Se density appears 2.1 Å above the outermost Fe layer over the octahedral vacancies in the hcp oxygen lattice (i.e., over the 1/3 of octahedral sites not occupied by Fe^{3+}). While some additional Se density is found on top of the Fe dimers, this is due to the use of a limited number of Fourier components in obtaining the density plot using Eq. (4). Comparable density is present at this site if f_H and P_H values calculated from a model with Se only over the octahedral vacancies are used as input for XSW imaging (calculations not shown). This provides a model-independent visualization of the structure with a spatial resolution of ∼1 Å, which is limited by the number of Fourier components that were measured.

Least-squares refinement of the Se position with respect to the surface unit cell were done to provide more precise, but model-dependent, structural information concerning the Se distribution. The position of maximum Se density from the directly inverted XSW image was used as an initial starting point (Table 2). The optimized Se position resulted in excellent agree-

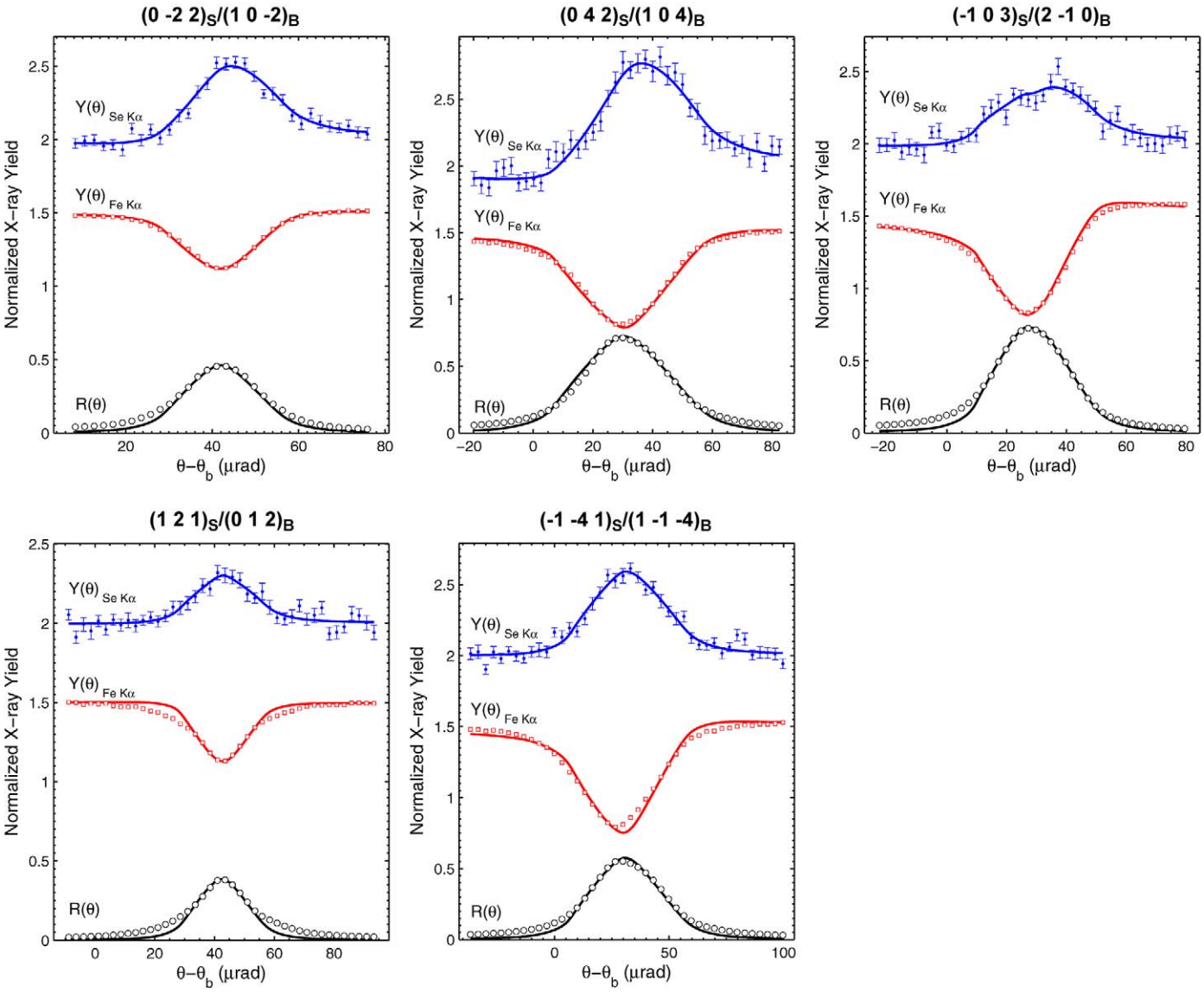

Fig. 2. Experimental $R(\theta)$ and $Y(\theta)$ data and fits to the XSW measurements of Se(IV) sorbed from a 10 μM solution onto the hematite (100) surface.

ment between the observed and calculated f_H and P_H values (Table 3). As there are two symmetry related Se sites in the surface unit cell, the position of Se in each site was constrained to preserve the symmetry of the surface (i.e., the relative motion along the three lattice directions were constrained as: $\Delta x_{\mathrm{Se1}} = -\Delta x_{\mathrm{Se2}}$, $\Delta y_{\mathrm{Se1}} = \Delta y_{\mathrm{Se2}}$, $\Delta z_{\mathrm{Se1}} = \Delta z_{\mathrm{Se2}}$). The positions of the two Se sites along $\mathbf{a}_s$ were fixed to $0.5\mathbf{a}_s$ as they consistently refined to this value but had unreasonably large least-squares errors when allowed to vary. The poor precision in the Se positions was a result of the symmetry constraints which fixed the mean Se position to $0.5\mathbf{a}_s$. Thus, motion along $\mathbf{a}_s$ only affected the f_H values (which had large errors) in the optimization by changing the geometrical factor, a (see Eq. (2)); P_H values were only affected by changes in the mean Se position. Relaxing the symmetry constraint along $\mathbf{a}_s$ (i.e., the constraint that $\Delta x_{\mathrm{Se1}} = -\Delta x_{\mathrm{Se2}}$ was removed) while keeping all other variables fixed resulted in a Se position of $0.49 \pm 0.01\mathbf{a}_s$ for both Se sites, suggesting that fixing the Se position along $\mathbf{a}_s$ to $0.5\mathbf{a}_s$ was valid for the full analysis. The symmetry constraint along $\mathbf{a}_s$ could not be relaxed in the full analysis because the number of variables would have exceeded the number of degrees of freedom. The ordered fraction, C, was determined to be 0.25, and, when combined with the measured surface coverage of 0.8 μmol m^{-2}, yields a coherent surface coverage of 0.2 μmol m^{-2} (0.12 Se atoms nm^{-2}). The remaining Se was likely adsorbed on defect sites, as disordered outer-sphere complexes, and/or in the diffuse layer.

In order to determine if the adsorption geometry changes at higher solution Se(IV) concentrations, additional XSW measurements were made in a 100 μM solution (Fig. 4). The fluorescence yields were similar to those observed at 10 μM Se(IV), producing comparable P_H values and slightly lower f_H value. This suggests that at this higher concentration Se binds in the same manner, with the reduction in f_H values due to the increased background Se fluorescence from the solution and additional outer-sphere or diffuse-layer species.

Table 2
Positions of Se (from XSW triangulation fitting), Fe, and O (from bulk crystal structure) in the hematite (100) surface unit cell

Atom	X (Å)	Y (Å)	Z (Å)[a]
		Adsorbed selenite	
Se[b]	2.52	4.5 ± 0.1	2.2 ± 0.1
Se[b]	2.52	11.4 ± 0.1	2.2 ± 0.1
		1st oxygen layer[c]	
O	3.29	1.15	1.33
O	1.54	3.44	1.45
O	3.29	5.73	1.57
O	1.75	8.02	1.33
O	3.50	10.31	1.45
O	1.75	12.60	1.57
		Iron layer[c]	
Fe	2.52	2.59	0
Fe	2.52	6.57	0
Fe	2.52	9.47	0
Fe	2.52	13.44	0
		2nd oxygen layer[c]	
O	0.98	1.15	0
O	4.34	3.44	0
O	0.77	5.73	−0.12
O	4.06	8.02	0
O	0.77	10.31	0.12
O	4.27	12.60	−0.12

[a] $Z = 0$ Å arbitrarily set to the iron layer.
[b] Two positions are related by symmetry.
[c] O and Fe positions are unrelaxed bulk atom locations for hematite.

Table 3
Comparison of measured and refined XSW results for Se in the bridging bidentate site

Reflection, $H(hkl)$		XSW data		Triangulation results		χ^2
Bulk	Surface	f_H	P_H	f_{opt}	P_{opt}	
$(1\,0\,\bar{2})$	$(0\,\bar{2}\,2)$	0.18	0.47	0.24(6)	0.53(3)	0.584
$(1\,0\,4)$	$(0\,4\,2)$	0.27	0.45	0.23(6)	0.48(5)	
$(2\,\bar{1}\,0)$	$(\bar{1}\,0\,3)$	0.32	0.81	0.22(6)	0.77(3)	
$(0\,1\,2)$	$(1\,2\,1)$	0.24	0.28	0.24(6)	0.24(3)	
$(1\,\bar{4}\,\bar{1})$	$(\bar{1}\,\bar{4}\,1)$	0.14	0.30	0.23(6)	0.29(4)	

The position of Se above the pairs of singly-coordinated oxygens on the surface demonstrates that Se binds in a bridging bidentate geometry (Fig. 5). Ignoring possible relaxation of the surface structure, this position results in Se–$O_{surface}$ distances of 1.6–1.7 Å and Se–Fe distances of 2.9–3.0 Å. Previous studies have shown that surface relaxations at hydrated min-

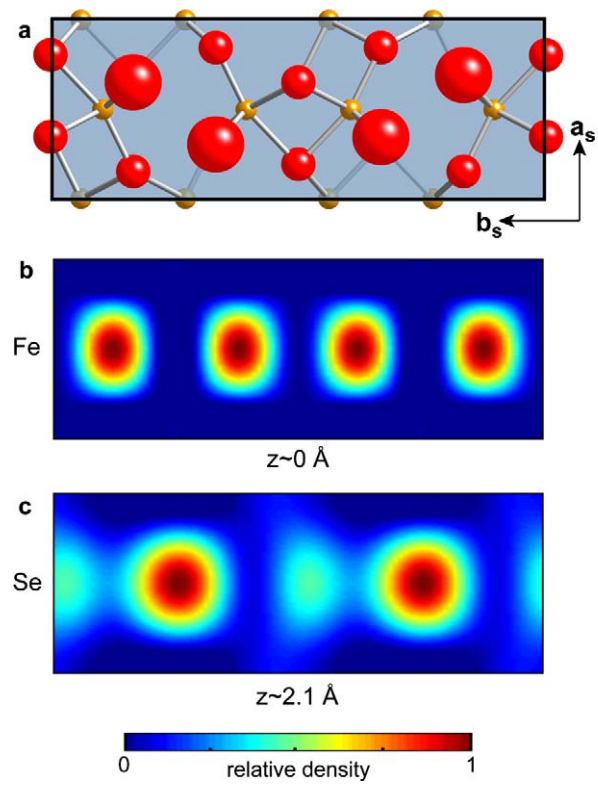

Fig. 3. Results of direct inversion of XSW data: (a) Top view of surface unit cell of hematite (100). The small spheres are iron, the medium sphere oxygen, and large spheres singly-coordinated oxygen sites on the surface. (b) Measured lateral distribution of Fe shown as a cut through maximum density plane. (c) Measured lateral distribution of Se shown as a cut through maximum density plane.

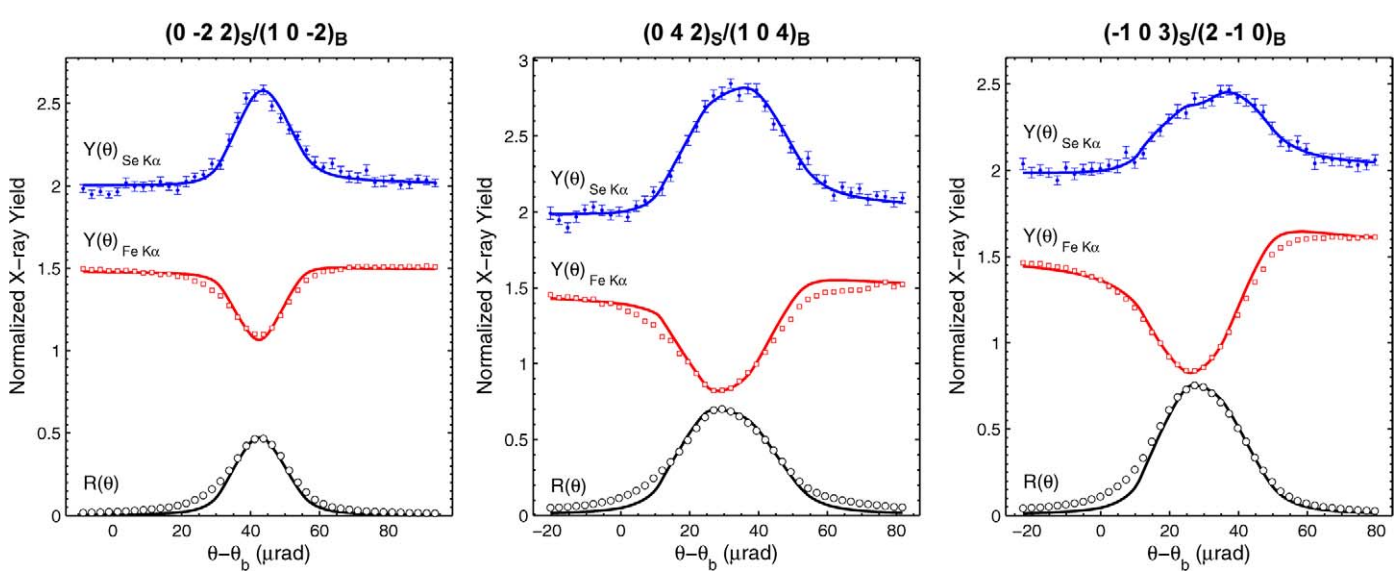

Fig. 4. Experimental $R(\theta)$ and $Y(\theta)$ data and fits to the XSW measurements of Se(IV) sorbed from a 100 μM solution onto the hematite (100) surface.

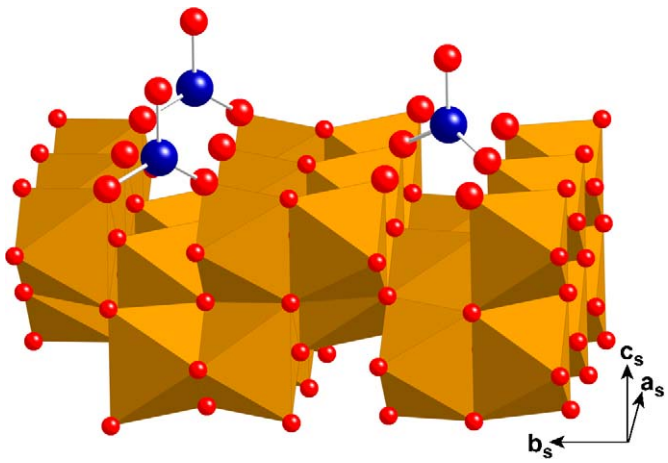

Fig. 5. Model of Se(IV) surface complexes on hematite (100) as determined from triangulation refinement of Se position. The selenite complex is shown as a planar complex (instead of trigonal pyramidal) as the XSW data provides no information regarding oxygen positions.

eral surfaces are relatively modest, typically <0.2 Å [40], and consequently these nominal bond lengths should approximate that of the actual surface complex. As XSW measurements cannot determine the position of the oxygen atoms in the hematite crystal or bound to the sorbed selenite molecules, it is unknown where the third (apical) oxygen atom on selenite is located. The trigonal pyramidal shape of selenite and the XSW-imaged localization of Se between the Fe atoms (and thus between two singly-coordinated oxygens) implies that this third oxygen must be above Se but off to one side of the $O_{surface}$–Se–$O_{surface}$ plane. The symmetry of the site suggests that there is no preferred direction of offset (i.e., offset of the apical oxygen in either direction is equally probable).

3.3. Se(IV) binding site preferences

Although sites were available for both edge-sharing and bridging bidentate selenite surface complexes to form, only the bridging complexes were observed. The lack of edge-sharing complexes may relate to the coordination of surface functional groups, as the bridging complexes only bond to the singly-coordinate oxygen sites, whereas formation of edge-sharing complexes also requires binding to doubly-coordinated oxygen sites. Singly- and doubly-coordinated oxygen sites on iron oxide surfaces have different acidity constants [41] and thus are expected to have different binding constants for selenite. Kinetic effects may also affect where selenite binds, as singly-coordinated oxygen groups have significantly faster exchange rates than doubly-coordinated groups [42]. Irrespective of the affinity of surface functional groups for selenite adsorption, cation–cation repulsion between Se and Fe may also make edge-sharing complexes (expected Se–Fe distance of ∼2.4 Å) less favorable than bridging complexes (Se–Fe distance of 2.9–3.0 Å) on the hematite (100) surface. However, the relative importance of functional group reactivity and exchange rates and cation–cation repulsion is difficult to assess without further study.

3.4. Comparison to past studies

Selenite has consistently been observed to form bidentate complexes on iron and aluminum oxide surfaces in EXAFS and infrared spectroscopic studies [31–34]. These complexes exclusively bind to these surfaces by bridging two adjacent apices of Fe(III) octahedra, except for the case of selenite sorbed on hydrous ferric oxide (HFO), where both bridging and edge-sharing complexes have been observed [33]. However, the Se–Fe distances predicted from the complexes observed in this study by XSW (2.9–3.0 Å) are significantly shorter than those seen in past EXAFS studies (3.38 Å), and would have likely been interpreted as evidence of the formation of bidentate edge-sharing complexes. This can be attributed to the orientation of the Fe(III) octahedra on the hematite (100) surface, which are rotated in a way that reduces the Se–Fe distance. This demonstrates that EXAFS spectra of adsorbates on mineral surfaces cannot always be interpreted correctly without a fundamental understanding of the geometry of surface functional groups.

4. Summary

Selenite (SeO_3^{2-}) adsorption on the hematite (100) surface was studied using XSW measurements. Selenite was found to adsorb in a bridging bidentate geometry on adjacent singly-coordinated oxygen groups. As doubly-coordinated oxygen groups were also exposed on the surface, exclusive binding to the singly-coordinates groups was likely due to differences in the reactivity or kinetics of these groups. The selenite adsorption geometry observed in this study was similar to geometries seen on related iron oxide phases in the past.

Acknowledgments

This work was supported by the Argonne National Laboratory Named Postdoctoral Fellowship Program and the Geosciences Research Program of the Office of Basic Energy Sciences, U.S. Department of Energy, through Contract W-31-109-ENG-38 to Argonne National Laboratory. The data were measured at beamline 12-ID-D of the Basic Energy Sciences Synchrotron Radiation Center (BESSRC/XOR), Advanced Photon Source (APS). The APS is national user facility operated on behalf of the DOE Office of Basic Energy Sciences. Comments from two anonymous reviewers improved this manuscript.

References

[1] G.E. Brown Jr., G.A. Parks, Int. Geol. Rev. 43 (2001) 963–1073.
[2] L. Cheng, P.F. Lyman, N.C. Sturchio, M.J. Bedzyk, Surf. Sci. 382 (1997) L690–L695.
[3] L. Cheng, N.C. Sturchio, J.C. Woicik, K.M. Kemner, P.F. Lyman, M.J. Bedzyk, Surf. Sci. 415 (1998) L976–L982.
[4] L. Cheng, P. Fenter, N.C. Sturchio, Z. Zhong, M.J. Bedzyk, Geochim. Cosmochim. Acta 63 (1999) 3153–3157.
[5] L. Cheng, N.C. Sturchio, M.J. Bedzyk, Phys. Rev. B 61 (2000) 4877–4883.
[6] L. Cheng, N.C. Sturchio, M.J. Bedzyk, Phys. Rev. B 63 (2001) 144104.
[7] S. Rihs, N.C. Sturchio, K. Orlandini, L.W. Cheng, H. Teng, P. Fenter, M.J. Bedzyk, Environ. Sci. Technol. 38 (2004) 5078–5086.

[8] N.C. Sturchio, R.P. Chiarello, L. Cheng, P.F. Lyman, M.J. Bedzyk, Y.L. Qian, H.D. You, D. Yee, P. Geissbuhler, L.B. Sorensen, Y. Liang, D.R. Baer, Geochim. Cosmochim. Acta 61 (1997) 251–263.
[9] J.G. Catalano, T.P. Trainor, P.J. Eng, G.A. Waychunas, G.E. Brown Jr., Geochim. Cosmochim. Acta 69 (2005) 3555–3572.
[10] G.A. Waychunas, T.P. Trainor, P.J. Eng, J.G. Catalano, G.E.J. Brown, J.A. Davis, J. Rogers, J.R. Bargar, Anal. Bioanal. Chem. 383 (2005) 12–27.
[11] P. Fenter, L. Cheng, S. Rihs, M. Machesky, M.J. Bedzyk, N.C. Sturchio, J. Colloid Interface Sci. 225 (2000) 154–165.
[12] Z. Zhang, P. Fenter, L. Cheng, N.C. Sturchio, M.J. Bedzyk, M. Predota, A. Bandura, J.D. Kubicki, S.N. Lvov, P.T. Cummings, A.A. Chialvo, M.K. Ridley, P. Benezeth, L. Anovitz, D.A. Palmer, M.L. Machesky, D.J. Wesolowski, Langmuir 20 (2004) 4954–4969.
[13] Z. Zhang, P. Fenter, L. Cheng, N.C. Sturchio, M.J. Bedzyk, M.L. Machesky, D.J. Wesolowski, Surf. Sci. 554 (2004) L95–L100.
[14] S.J. Hamilton, Sci. Total Environ. 326 (2004) 1–31.
[15] A.S. Templeton, T.P. Trainor, A.M. Spormann, G.E. Brown Jr., Geochim. Cosmochim. Acta 67 (2003) 3547–3557.
[16] C.P. Schulthess, Z.Q. Hu, Soil Sci. Soc. Am. J. 65 (2001) 710–718.
[17] C.H. Wu, S.L. Lo, C.F. Lin, Colloids Surf. A 166 (2000) 251–259.
[18] K. Saeki, S. Matsumoto, Commun. Soil Sci. Plant Anal. 29 (1998) 3061–3072.
[19] K. Saeki, S. Matsumoto, R. Tatsukawa, Soil Sci. 160 (1995) 265–272.
[20] K. Saeki, S. Matsumoto, Commun. Soil Sci. Plant Anal. 25 (1994) 2147–2158.
[21] K.M. Parida, B. Gorai, N.N. Das, S.B. Rao, J. Colloid Interface Sci. 185 (1997) 355–362.
[22] K.M. Parida, B. Gorai, N.N. Das, J. Colloid Interface Sci. 187 (1997) 375–380.
[23] C. Papelis, P.V. Roberts, J.O. Leckie, Environ. Sci. Technol. 29 (1995) 1099–1108.
[24] C. Papelis, Environ. Sci. Technol. 29 (1995) 1526–1533.
[25] M.M. Ghosh, C.D. Cox, J.R. Yuanpan, Environ. Prog. 13 (1994) 79–88.
[26] P.C. Zhang, D.L. Sparks, Environ. Sci. Technol. 24 (1990) 1848–1856.
[27] D.D. Hansmann, M.A. Anderson, Environ. Sci. Technol. 19 (1985) 544–551.
[28] J.W. Bowden, S. Nagarajah, N.J. Barrow, A.M. Posner, J.P. Quirk, Aust. J. Soil Res. 18 (1980) 49–60.
[29] S.S.S. Rajan, J. Soil Sci. 30 (1979) 709–718.
[30] F.J. Hingston, A.M. Posner, J.P. Quirk, in: J.W.J. Weber, E. Matijevic (Eds.), Adsorption from Aqueous Solution. American Chemical Society, Washington, DC, 1968, pp. 82–90.
[31] C.M. Su, D.L. Suarez, Soil Sci. Soc. Am. J. 64 (2000) 101–111.
[32] C. Papelis, G.E. Brown Jr., G.A. Parks, J.O. Leckie, Langmuir 11 (1995) 2041–2048.
[33] A. Manceau, L. Charlet, J. Colloid Interface Sci. 168 (1994) 87–93.
[34] K.F. Hayes, A.L. Roe, G.E. Brown, K.O. Hodgson, J.O. Leckie, G.A. Parks, Science 238 (1987) 783–786.
[35] T.P. Trainor, A.M. Chaka, P.J. Eng, M. Newville, G.A. Waychunas, J.C. Catalano, G.E. Brown Jr., Surf. Sci. 573 (2004) 204–224.
[36] M.J. Bedzyk, G.M. Bommarito, M. Caffrey, T.L. Penner, Science 248 (1990) 52–56.
[37] M.J. Bedzyk, L. Cheng, Rev. Mineral. Geochem. 49 (2002) 221–266.
[38] L. Cheng, P. Fenter, M.J. Bedzyk, N.C. Sturchio, Phys. Rev. Lett. 90 (2003).
[39] L.W. Finger, R.M. Hazen, J. Appl. Phys. 51 (1980) 5362–5367.
[40] P. Fenter, N.C. Sturchio, Prog. Surf. Sci. 77 (2004) 171–258.
[41] T. Hiemstra, P. Venema, W.H. van Riemsdijk, J. Colloid Interface Sci. 184 (1996) 680–692.
[42] W.H. Casey, T.W. Swaddle, Rev. Geophys. 41 (2003) 1008.